NATIONAL INSTITUTE FOR FUSION SCIENCE

Ion Temperature Gradient Modes in
Toroidal Helical Systems

T. Kuroda, H. Sugama, R. Kanno and M. Okamoto

RESEARCH REPORT
NIFS Series

NAGOYA, JAPAN

Ion Temperature Gradient Modes in Toroidal Helical Systems

T. KURODA , H. SUGAMA[1] , R. KANNO[1] , and M. OKAMOTO[1]

Graduate University for Advanced Studies, Toki 509-5292

[1] *National Institute for Fusion Science, Toki 509-5292*

Linear properties of ion temperature gradient (ITG) modes in helical systems are studied. The real frequency, growth rate, and eigenfunction are obtained for both stable and unstable cases by solving a kinetic integral equation with proper analytic continuation performed in the complex frequency plane. Based on the model magnetic configuration for toroidal helical systems like the Large Helical Device (LHD), dependences of the ITG mode properties on various plasma equilibrium parameters are investigated. Particularly, relative effects of ∇B-curvature drifts driven by the toroidicity and by the helical ripples are examined in order to compare the ITG modes in helical systems with those in tokamaks.

§1. Introduction

The ion temperature gradient (ITG) modes are one of drift wave instabilities. Many works have been done on the ITG modes since they are considered a cause of the anomalous ion heat transport in high temperature core regions of tokamak plasmas.[1,2] Recently, the Large Helical Device (LHD)[3] of National Institute for Fusion Science succeeded in generation of the high ion temperature $T_i(0) \geq 3$ keV by means of neutral beam injection.[4] Observed ion temperature profiles are steeper than density profiles. Thus, the ITG modes are expected to become unstable and drive the anomalous transport in helical systems as well.

Since tokamaks have the non-uniformity of the magnetic field (toroidicity), the magnetic ∇B-curvature drift motions of particles occur and the convective mechanism causes the instability which is more unstable than that driven by the acoustic mechanism in slab systems.[5,6] In helical systems such as LHD, the drift motions are driven not only by the toroidicity but also by the helicity (helical ripples). The magnetic field strength for the large aspect ratio helical system is given by

$$B/B_0 = 1 - \epsilon_t \cos\theta - \epsilon_h \cos(L\theta - M\zeta), \qquad (1.1)$$

where B_0 is the magnetic field strength on the magnetic axis, θ and ζ represent the poloidal and the toroidal angles, respectively, and L and M are the poloidal and toroidal period numbers of the helical fields, respectively. For example, $L = 2$, $M = 10$ for the LHD and $L = 2$, $M = 8$ for the Compact Helical System (CHS).[7] Here, $\epsilon_t = r/R \ll 1$ (r: the minor radius, R: the major radius) and $\epsilon_h(\propto r^L)$ represent the parameters associated with the toroidicity and helicity, respectively.

For tokamaks ($\epsilon_h = 0$), the ITG mode is localized like a Gaussian function in the outer region of the torus $-\pi/2 < \theta < \pi/2$, which is called the bad curvature region since the ion drift motions in this region destabilize the ITG mode. This local destabilization is brought by

the toroidicity. For helical systems ($\epsilon_h \neq 0$), the equilibrium depends not only on θ but also on ζ, and the distribution of bad curvature regions become more complicated due to the helicity combined with the toroidicity. Another important feature of the helical systems is the negative magnetic shear in contrast with the positive magnetic shear of the conventional tokamaks. These characteristics are expected to bring about different effects on the ITG mode.

In this work, in order to to take account of kinetic effects such as wave-particle interactions and finite ion gyroradii, we use the ion gyrokinetic equation[8,9] to obtain the dispersion relation and the mode structure of the linear electrostatic ITG mode in the LHD-like helical system, which is compared with the tokamak ITG mode. Recently, similar gyrokinetic analyses have been done on the ITG mode in the helias configuration[10] and in the quasi-axisymmetric stellarator.[11] Here, assuming the low β(= the ratio of the plasma pressure to the magnetic pressure) large aspect ratio toroidal plasma, we clarify the effects of the ion ∇B-curvature drift motion in the helical system with the model magnetic field given by eq. (1.1).

The rest of this work is organized as follows. In § 2, the dispersion relation of the linear ITG mode in the helical system is derived as a kinetic integral equation from the ion gyrokinetic equation, the adiabatic electron assumption, and the quasineutrality condition. In § 3, results from numerical solutions of the integral equation are presented to show dependences of the ITG mode properties on various plasma equilibrium parameters such as the helical ripple intensity, safety factor, magnetic shear, ballooning angle, poloidal wavenumber, temperature and density gradients. In § 4, conclusions are given.

§2. Dispersion Relation of ITG Modes

In this section, a kinetic integral equation to give the dispersion relation of the ITG mode in the helical system is derived. Here, we consider the linear electrostatic ITG

mode in a high temperature plasma and neglect collisional effects on the dispersion relation. The electrostatic potential perturbation is written as $\phi \propto \exp(-i\omega t)$ with a complex frequency $\omega = \omega_r + i\gamma$. Electrons are assumed to adiabatically respond to the electrostatic perturbation. Then, the electron density perturbation is given by $\delta n_e = (e\phi/T_e)n_0$, where n_0 denotes the equilibrium density, $-e$ represents the electron charge, and T_e is the equilibrium electron temperature.

The ion distribution function is written as $f_i = n_0 F_M + \delta f_i$. Here, the equilibrium part is assumed to be given by the Maxwellian distribution function $F_M \equiv \pi^{-3/2} v_{Ti}^{-3} \exp(-v^2/v_{Ti}^2)$, where the ion thermal velocity is give by $v_{Ti} \equiv (2T_i/m_i)^{1/2}$ with the equilibrium ion temperature T_i. The perturbation part is given by $\delta f_i = -(e\phi/T_i)n_0 F_M + h \exp(-i \, \boldsymbol{k}_\perp \cdot \boldsymbol{\rho})$, where $\boldsymbol{\rho} \equiv \boldsymbol{b} \times \boldsymbol{v}/\Omega_i$ ($\boldsymbol{b} \equiv \boldsymbol{B}/B$) is the ion gyroradius vector, and $\Omega_i \equiv eB/(m_i c)$ is the ion gyrofrequency. The non-adiabatic part of the distribution function h is determined by the linear gyrokinetic equation[8,9]

$$(\omega - \omega_D + iv_\parallel \boldsymbol{b} \cdot \nabla) h = (\omega - \omega_{*T}) \frac{e\phi}{T_i} J_0(k_\perp \rho) \, n_0 F_M, \tag{2.1}$$

where $\omega_D = \boldsymbol{k}_\perp \cdot \boldsymbol{v}_D$, $\omega_{*T} = \omega_{*i}[\, 1 + \eta_i \{ (v/v_{Ti})^2 - 3/2 \} \,]$, $\eta_i \equiv L_n/L_{Ti}$, $L_n \equiv -n_0[dn_0(r)/dr]^{-1}$, and $L_n \equiv -T_i[dT_i(r)/dr]^{-1}$. Here, $\boldsymbol{v}_D = \Omega_i^{-1} (v_\parallel^2 + v_\perp^2/2) \, \boldsymbol{b} \times B^{-1} \nabla B$ is the ion ∇B-curvature drift velocity, J_0 is the Bessel function of order zero, $\omega_{*i} \equiv -\tau_e^{-1} \omega_{*e}$ is the ion diamagnetic drift frequency, $\tau_e \equiv T_e/T_i$ is the ratio between the electron and ion temperatures, $\omega_{*e} \equiv ck_\theta T_e/(eBL_n)$ is the electron diamagnetic drift frequency, and k_θ is the poloidal wavenumber.

In the present work, following Dong et al.[12] and Romanelli,[13] effects of the magnetic configuration are taken into account only through the ion ∇B-curvature drift motion. Trapped particle effects are neglected here since mainly the passing ions drive the ITG modes. We consider a large aspect ratio and low β toroidal system, for which the magnetic field strength is given by eq. (1.1). Then, the ion ∇B-curvature drift frequency is given by

$$\omega_D = 2(L_n/r)\omega_{*i}(\, v_\parallel^2 + v_\perp^2/2 \,)/v_{Ti}^2$$

$$\times \left[\; \epsilon_t \{ \cos\theta + \hat{s}(\theta - \theta_k) \sin\theta \} \right.$$

$$\left. + L\epsilon_h \{ \cos(L\theta - M\zeta) + \hat{s}(\theta - \theta_k) \sin(L\theta - M\zeta) \} \; \right], \tag{2.2}$$

where $\hat{s} = (r/q)dq/dr$ is the magnetic shear parameter.

In eq. (2.1), the ballooning representation[14,15] is used, and the perpendicular wavenumber vector is written as $\boldsymbol{k}_\perp = k_\alpha(\nabla\alpha + \theta_k \nabla q)$. Here, $q(r)$ is the safety factor, $\alpha = \zeta - q\theta$ is the label of the magnetic field line, and $k_\alpha = -n$ represents the toroidal mode number, which is related to the poloidal wavenumber as $k_\theta = nq/r$. Using the independent variables (q, α, θ) as the spatial coordinates, (2.1) becomes the ordinary differential equation with respect to θ. Integrating the gyrokinetic equation (2.1) along the field line with the boundary conditions $h(\theta \to \pm\infty) = 0$, and substituting it into the quasineutrality

condition $\delta n_i = -(e\phi/T_i)n_0 + \int d^3v J_0(k_\perp \rho)h = \delta n_e = (e\phi/T_e)n_0$, we obtain the integral equation,

$$\left(1 + \frac{T_e}{T_i}\right) \phi(\omega, k) = \int_{-\infty}^{+\infty} \frac{dk'}{\sqrt{2\pi}} K(k, k')\phi(\omega, k') \tag{2.3}$$

with

$$K(k, k') = -i \int_{-\infty}^0 \omega_{*e} d\tau \frac{\sqrt{2} e^{-i\omega\tau}}{\sqrt{a}(1 + a)\sqrt{\lambda}} e^{-(k-k')^2/4\lambda}$$

$$\times \left[\frac{\omega}{\omega_{*e}} \tau_e + 1 - \frac{3}{2}\eta_i + \frac{\eta_i(k - k')^2}{4a\lambda} + \frac{2\eta_i}{(1 + a)} \right.$$

$$\left. \left(1 - \frac{k_\perp^2 + k_\perp'^2}{2(1 + a)\tau_e} + \frac{k_\perp k_\perp'}{(1 + a)\tau_e} \frac{I_1}{I_0}\right) \right] \Gamma_0(k_\perp, k_\perp'), \tag{2.4}$$

where $I_j = I_j(\, k_\perp k_\perp'/[(1 + a)\tau_e] \,)$ ($j = 0, 1$) are the modified Bessel functions of j-th order, $\lambda = (\omega_{*e}\tau)^2(\hat{s}\epsilon_n/q)^2/\tau_e a$, $\epsilon_n = L_n/R$, $k = \hat{s}k_\theta(\theta - \theta_k)$, $k' = \hat{s}k_\theta(\theta' - \theta_k)$, $\Gamma_0(k_\perp, k_\perp') = I_0(\, k_\perp k_\perp'/[(1 + a)\tau_e] \,) \exp[-(k_\perp^2 + k_\perp'^2)/2\tau_e(1 + a)]$, $k_\perp^2 = k_\theta^2 + k^2$, $k_\perp'^2 = k_\theta^2 + k'^2$, and

$$a = 1 - i2(L_n/r)\tau_e^{-1}\omega_{*e}\tau/(\theta - \theta')$$

$$\times \left(\; \epsilon_t \left[(\hat{s} + 1)(\sin\theta - \sin\theta') \right.\right.$$

$$\left. -\hat{s}\{(\theta - \theta_k)\cos\theta - (\theta' - \theta_k)\cos\theta'\} \right]$$

$$+ (L\epsilon_h(L - Mq)^{-1}) \left[\; \{\hat{s}(L - Mq)^{-1} + 1\} \right.$$

$$\times \{\sin[(L - Mq)\theta - M\alpha] - \sin[(L - Mq)\theta' - M\alpha]\}$$

$$- \hat{s} \Big\{ (\theta - \theta_k)\cos(\, (L - Mq)\theta - M\alpha \,)$$

$$\left.\left. -(\theta' - \theta_k)\cos(\, (L - Mq)\theta' - M\alpha \,) \Big\} \; \right] \; \right). \tag{2.5}$$

Here, the wavenumber variables k_θ, k, and k' are normalized by ρ_s^{-1} ($\rho_s = \sqrt{2T_e/m_i}/\Omega_i$) and $\epsilon_h(r) \propto r^L$ is used.

The integral equation (2.3) with the boundary conditions $\phi(\theta \to \pm\infty) = 0$ determines the complex-valued eigenfrequency and eigenfunction of the ITG mode for the helical system. If we put $\epsilon_h = 0$, the integral ITG mode equation (2.3) with eqs. (2.4) and (2.5) reduces to the one given by Dong, et al. for the tokamak case.[12] Compared to the tokamak case, the dispersion relation for the helical system depends on additional parameters ϵ_h/ϵ_t, L, M, and α, Then, the eigenfrequency is written as

$$\omega = \omega(q, \hat{s}, \theta_k, \alpha, k_\theta, \eta_i, \epsilon_n, \tau_e, \epsilon_h/\epsilon_t, L, M). \tag{2.6}$$

In the next section, eq. (2.3) is numerically solved to investigate dependences of the ITG mode real frequency, growth rate, and structure on these parameters. Our numerical code can calculate both positive and negative growth rates with proper analytic continuation of the dispersion relation in the complex frequency plane.[16-18] Detailed procedures for the analytic continuation are shown in Ref. 18).

§3. Numerical Results

In this section, we numerically solve the integral equation (2.3) with the boundary conditions $\phi(\theta \to \pm\infty) = 0$ to obtain the real frequency, growth rate, and eigenfunction of the ITG mode for the helical system with $L = 2$ and $M = 10$ (corresponding to the LHD case). As the standard parameters for the numerical calculation, we use $L = 2$, $M = 10$, $\epsilon_h/\epsilon_t = 1$, $q = 2$, $\hat{s} = -1$, $\tau_e = 1$, $\eta_i = 3$, $\epsilon_n = 0.3$, $\theta_k = 0$, $\alpha = 0$, and $k_\theta \rho_{Ti} = 0.65$. Here, $\rho_{Ti} = v_{Ti}/\Omega_i$ is the ion thermal gyroradius. These parameters except for ϵ_n are chosen such that they correspond to those at the magnetic surface $r/a = 0.6$ of the typical NBI-heated hydrogen plasma in LHD with $B = 2.75T$, $T_i(0.6a) = T_e(0.6a) = 1.6keV$, $n(0.6a) = 0.7 \times 10^{19}m^{-3}$, $\beta(0.6a) = 0.12\%$, $R = 3.6m$, $a = 0.6m$, and $L_{Ti} = 0.36m$. Very flat density profiles ($\epsilon_n = L_n/R \sim \infty$) are observed in the LHD[19] although we use $\epsilon_n = 0.3$ ($L_n \sim 1m$) here. The flat density profile case is treated later in § 3.8. The field line $\alpha = 0$ passes through the point where magnetic field strength B has its smallest value on the magnetic flux surface. Also, $\theta_k = 0$ is the poloidal angle where the radial wavenumber k_r vanishes since $k_r = \hat{s}k_\theta(\theta - \theta_k)$. Therefore, the ITG mode is considered to become the most unstable for $\alpha = 0$ and $\theta_k = 0$. As seen later, the growth rate has a peak around the poloidal wavenumber $k_\theta\rho_{Ti} = 0.65$. Then, using the LHD parameters shown above, we obtain $\omega_{*e} = 1.8 \times 10^5 sec^{-1}$, $\omega_{*e}\epsilon_n = 0.54 \times 10^5 sec^{-1}$, and $\lambda_\theta = 2\pi/k_\theta = 2.0 \times 10^{-2}m$ for $k_\theta\rho_{Ti} = 0.65$.

Here, we write the nondimensional factor, which represents the poloidal structure of the ∇B-curvature drift frequency, as

$$G(\theta) = \cos\theta - \hat{s}(\theta - \theta_k)\sin\theta$$
$$-(\epsilon_h/\epsilon_t)L\left[\cos\left((L - Mq)\theta - M\alpha\right)\right.$$
$$\left. -\hat{s}(\theta - \theta_k)\sin\left((L - Mq)\theta - M\alpha\right)\right],$$
$$(3.1)$$

which we call a curvature factor hereafter. It should be noted that, for $k_\theta > 0$, the sign of $G(\theta)$ is opposite to that of ω_D in eq. (2.2) because $L_n\omega_{*i} < 0$. For $G(\theta) > 0$, the poloidal ion ∇B-curvature drift motion at the poloidal angle θ is in the same direction as the ion diamagnetic rotation. Such a poloidal region is called a bad curvature region because the destabilization of the modes occurs there. On the other hand, in the good curvature region ($G(\theta) < 0$), the ion magnetic drift is in the direction of the electron diamagnetic direction, and the modes are stabilized. For the helical system with $\epsilon_h/\epsilon_t \sim 1$ and $L \ll Mq$, the connection length between adjacent good and curvature regions is roughly given by Rq/M.

In the following subsections, we investigate dependences of the ITG mode properties on the equilibrium parameters in the regions around the standard parameters.

3.1 Helical ripple effects

Effects of the parameter ϵ_h/ϵ_t on the normalized real frequency ω_r/ω_{*e} [$\omega_r = \text{Re}(\omega)$], the normalized growth rate γ/ω_{*e} [$\gamma = \text{Im}(\omega)$], and the eigenfunction $\phi(\theta) = \phi_r + i\phi_i$ are shown in Figs. 1 and 2. The parameters used here are the same as the standard ones (see the first paragraph of this section) except for ϵ_h/ϵ_t. The case of $\eta_i = 4$ is also plotted in Fig. 1. No helical ripple case $\epsilon_h/\epsilon_t = 0$ corresponds to the negative shear tokamak. With increasing ϵ_h/ϵ_t, the fine spatial structure of helical ripples appears and the connection length between adjacent good and bad curvature regions becomes shorter as seen from $G(\theta)$ in Fig. 2. The large helical ripples can produce the good curvature region even in the outside of the torus. Then, the eigenfunction enters not only the bad curvature region but also the good curvature region. That results in the monotonic decrease of the growth rate γ with increasing ϵ_h/ϵ_t. On the other hand, the real frequency are weakly dependent on ϵ_h/ϵ_t, and keeps the negative sign, which implies the wave propagation in the ion diamagnetic direction.

Using the ballooning transform,[14]

$$\phi(r, \theta, \zeta)$$
$$= \sum_{j=-\infty}^{+\infty} \phi(\theta + 2\pi j)\exp[-in\{\zeta - q(r)(\theta + 2\pi j - \theta_k)\}],$$
$$(3.2)$$

we obtain the three dimensional distribution of the electrostatic potential $\phi(r, \theta, \zeta)$ from the one dimensional eigenfunction $\phi(\theta)$. In eq. (3.2), the radial dependence of $\phi(r, \theta, \zeta)$ are considered only through $q(r) \simeq q(r_s) + (\hat{s}q/r)(r - r_s)$ where r_s denotes the radial position of a given magnetic surface. Thus, the three dimensional structure give by eq. (3.2) is valid only in the neighborhood of the magnetic surface $r = r_s$. The potential distribution $\phi(r, \theta, \zeta)$ in the region ($1.8 \leq q \leq 2.2$, $0 \leq \zeta \leq 2\pi/5$) around the $q = 2$ surface, which corresponds to Fig. 2 (b-1) (the case of the standard parameters), is shown in Fig. 3, where the toroidal mode number is determined from $k_\theta = nq/r = 0.65\rho_{Ti}^{-1}$ as $n = 56$. We can see the poloidal localization of the mode structure accompanied with its radial extension.

3.2 Effects of the safety factor q

Figure 4 shows the normalized real frequency and growth rate as a function of the safety factor q (the rotational transform is given by $\iota = q^{-1}$). The parameters used here are the same as the standard ones (see the first paragraph of this section) except for q. Also, the negative shear tokamak case with the same parameters except for $\epsilon_h/\epsilon_t = 0$ is plotted in Fig. 4. The growth rate for the helical case ($\epsilon_h/\epsilon_t = 1$) is smaller than for the tokamak case due to the stabilization effect of the helical ripples as explained in the previous subsection. We can see that the real frequency is weakly dependent on q although the growth rate becomes smaller for smaller q (larger ι) for both the tokamak and the helical cases. As seen in Fig. 2, for both cases, the width of the eigenfunction along the field line scales by the connection length Rq between inside and outside of the torus. Therefore, the effective
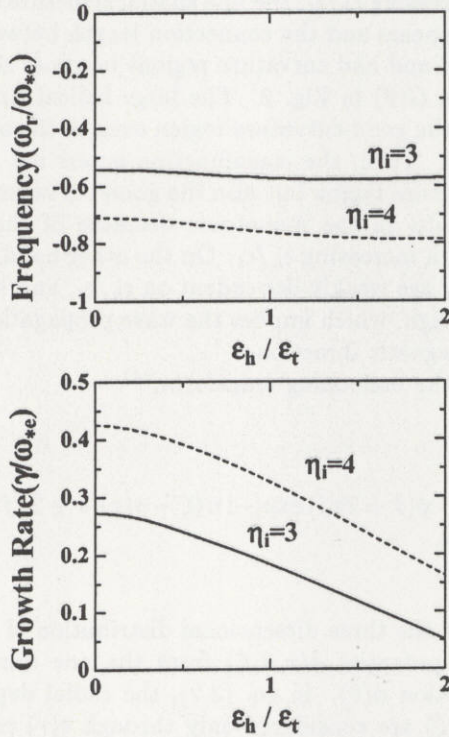
Tohru KURODA , Hideo SUGAMA , RyutaroKANNO and Masao OKAMOTO

Fig. 1. Normalized real frequency ω_r/ω_{*e} (top) and growth rate γ/ω_{*e} (bottom) as a function of ϵ_h/ϵ_t for $L = 2$, $M = 10$, $q = 2$, $\hat{s} = -1$, $\theta_k = 0$, $\alpha = 0$, $\eta_i = 3, 4$, $\epsilon_n = 0.3$, and $k_\theta\rho_{Ti} = 0.65$.
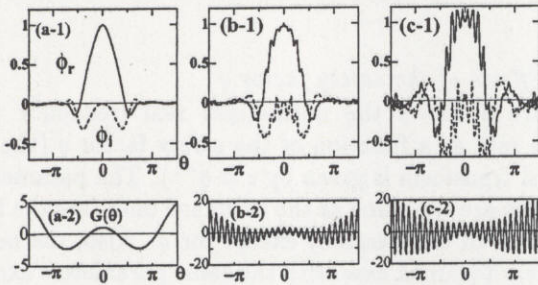

Fig. 2. Eigenfunction $\phi(\theta) = \phi_r + i\,\phi_i$ and curvature factor $G(\theta)$ for $\epsilon_h/\epsilon_t = 0$ (a-1,2), $\epsilon_h/\epsilon_t = 1$ (b-1,2), and $\epsilon_h/\epsilon_t = 2$ (c-1,2). Here, $\theta = 0$ and $\theta = \pm\pi$ correspond to the outermost and innermost points on the toroidal magnetic surface, respectively. The other parameters are $L = 2$, $M = 10$, $q = 2$, $\hat{s} = -1$, $\theta_k = 0$, $\alpha = 0$, $\eta_i = 3$, $\epsilon_n = 0.3$, and $k_\theta\rho_{Ti} = 0.65$.

Electrostatic fluctuation ϕ
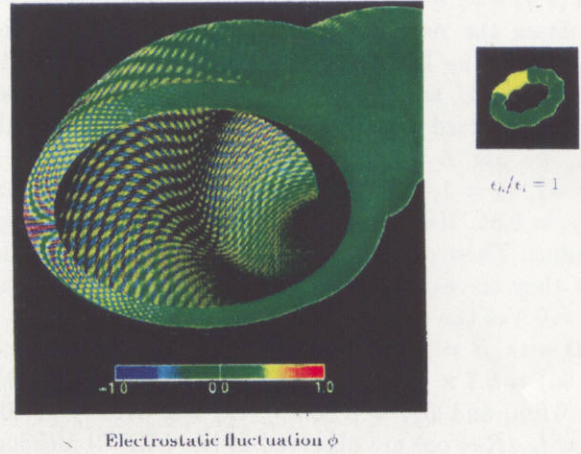
Fig. 3. The three dimensional distribution of the real part of the potential function $\phi(r, \theta, \zeta)$ in the region ($1.8 \leq q \leq 2.2$, $0 \leq \zeta \leq 2\pi/5$) around the $q = 2$ surface. The potential values are shown by colors. The same parameters as in Fig. 2 (b-1) are used.

parallel wavelength $k_\parallel^{-1} \sim Rq$ and the parallel phase velocity $\omega/k_\parallel$ of the mode are reduced when q decreases. Then, the Landau damping becomes stronger, which is considered a stabilization mechanism for smaller q.

3.3 Effects of the magnetic shear $\hat{s}$

Figure 5 shows the normalized real frequency and growth rate as a function of the magnetic shear parameter $\hat{s}$. The parameters used here are the same as the standard ones (see the first paragraph of this section) except for $\hat{s}$. The negative shear tokamak case with the same parameters except for $\epsilon_h/\epsilon_t = 0$ is plotted in Fig. 5. It should be noted that the validity of the ballooning representation is lost in the limit $\hat{s} \to 0$ although the real frequency and growth rate for $\hat{s} = 0$ are plotted in Fig. 5. We see that, for both tokamak and helical cases, the growth rate has a peak at $\hat{s}_p \simeq 0.42$ in the positive shear region. As $|\hat{s} - \hat{s}_p|$ increases, the growth rate monotonically decreases, and the growth rate for negative shear $\hat{s} < 0$ is smaller than for positive shear $\hat{s} > 0$ with the same $|\hat{s}|$. The same tendency has been observed in the works on negative shear tokamaks.[18, 20, 21] The real frequency for $\hat{s} > 0$ takes more negative values than for $\hat{s} < 0$. Figure 6 shows the eigenfunction $\phi(\theta) = \phi_r + i\phi_i$ and the curvature factor $G(\theta)$ for both tokamak and helical cases with $\hat{s} = 1, 0.5, -1$. It is understood from Fig. 6 that the reduction of the growth rate for the negative shear case is due to the reduction of the bad curvature region in the torus outside.

3.4 Effects of the ballooning angle θ_k

Since $k_r = \hat{s}k_\theta(\theta - \theta_k)$, θ_k represents the poloidal angle, at which the radial wavenumber k_r vanishes and accordingly the finite gyroradius stabilization effect is weakest.
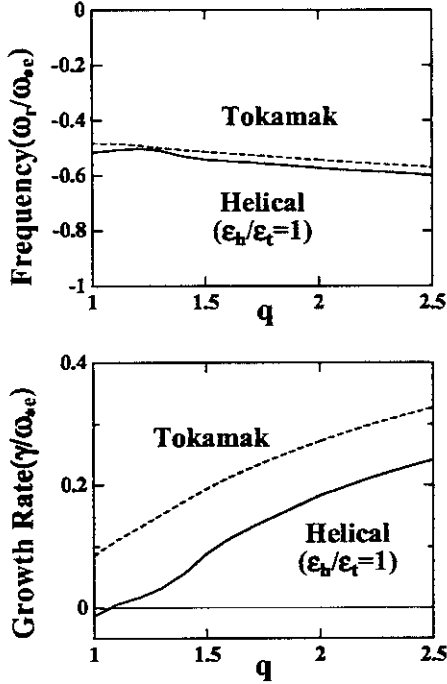
Fig. 4. Normalized real frequency ω_r/ω_{*e} (top) and growth rate γ/ω_{*e} (bottom) as a function of the safety factor q for $L = 2$, $M = 10$, $\hat{s} = -1$, $\epsilon_h/\epsilon_t = 1$, $\theta_k = 0$, $\alpha = 0$, $\eta_i = 3$, $\epsilon_n = 0.3$, and $k_\theta \rho_{Ti} = 0.65$. The negative shear tokamak case with the same parameters except for $\epsilon_h/\epsilon_t = 0$ is plotted by the dotted line.
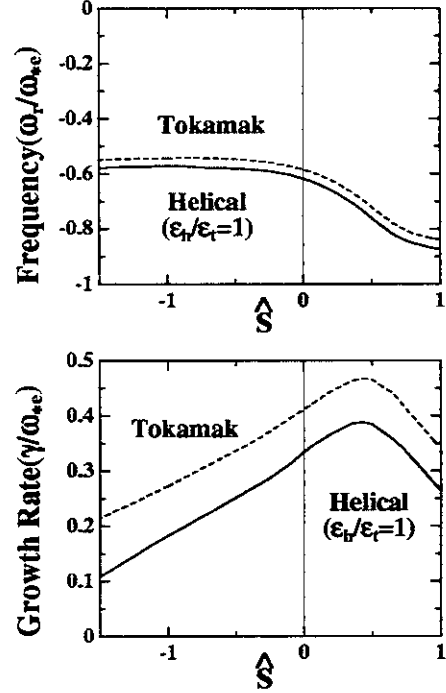
Fig. 5. Normalized real frequency ω_r/ω_{*e} (top) and growth rate γ/ω_{*e} (bottom) as a function of the magnetic shear parameter $\hat{s}$ for $L = 2$, $M = 10$, $q = 2$, $\epsilon_h/\epsilon_t = 1$, $\theta_k = 0$, $\alpha = 0$, $\eta_i = 3$, $\epsilon_n = 0.3$, and $k_\theta \rho_{Ti} = 0.65$. The negative shear tokamak case with the same parameters except for $\epsilon_h/\epsilon_t = 0$ is plotted by the dotted line.

Thus, the mode tends to be poloidally localized around $\theta = \theta_k$. Also, when we consider a rotating plasma, it is important to take account of θ_k-dependence.[22-25] Figure 7 shows the normalized real frequency and growth rate as a function of θ_k. The parameters used here are the same as the standard ones (see the first paragraph of this section) except for θ_k. The negative shear tokamak case with $\epsilon_h/\epsilon_t = 0$ is also plotted in Fig. 7. It is seen in Fig. 7 that the real frequency is a slightly decreasing function of θ_k, which is a contrast to the case of the positive shear tokamak.[18] The growth rate of the helical ITG mode is always smaller than that of the corresponding tokamak ITG mode. They are both significantly reduced for $\theta_k \to \pi/2$ when the toroidal destabilization does not work well at the poloidal angle of the mode localization. For the parameters used here, the helical ITG mode structure has a similar width along the field line to that of the tokamak ITG mode, and therefore the poloidal mode shift due to the θ_k-variation affects the stability more effectively than the α-variation as shown in the next subsection.

3.5 Effects of the field line label α

The non-axisymmetry of the helical system causes the α-dependence of the linear mode properties. We vary α within a toroidal period $-\pi/M < \alpha < \pi/M$ ($M = 10$). Figure 8 shows the normalized real frequency and growth rate as a function of α. The parameters used here are the same as the standard ones (see the first paragraph of this section) except for α. We find that there is little dependence of the real frequency and growth rate on α. The curvature factor $G(\theta)$ is shown for $\alpha = 0, \pi/20, \pi/10$ in Fig. 9. The weak α-dependence shown in Fig. 8 is interpreted as follows. In our model of the magnetic field strength, eq. (1.1), variation of α is reflected in the helical ripple phase shift. Since the ITG mode for the standard parameters extends in the whole region of the torus outside $(-\pi/2 < \theta < \pi/2)$ like for the tokamak case, the small helical phase shift $(< 2\pi/M)$ caused by varying α changes little the average effect of the helical ripples on the mode stability as expected from Fig. 9. However, we should note that our magnetic field model is valid only for low β values and that high β effects such as the Shafranov shift are not treated in it. If these high β effects are included, larger α-dependence may occur.
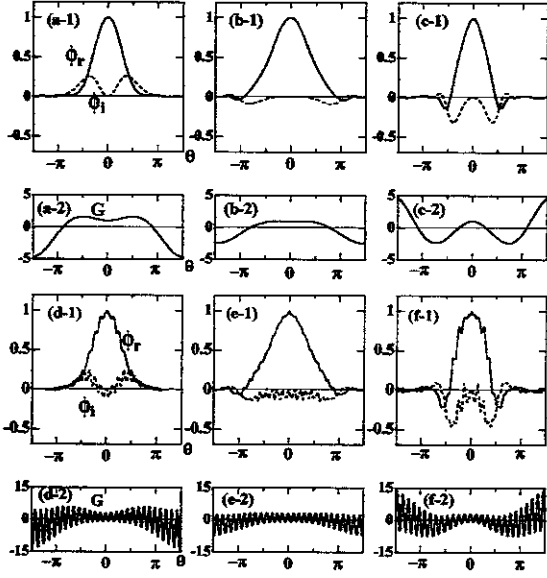
Fig. 6. Eigenfunction $\phi(\theta) = \phi_r + i\phi_i$ and curvature factor $G(\theta)$ for the tokamak cases $\epsilon_h/\epsilon_t = 0$ with $\hat{s} = 1$ (a-1, 2), $\hat{s} = 0.5$ (b-1, 2), $\hat{s} = -1$ (c-1, 2), and for the helical cases $\epsilon_h/\epsilon_t = 1$ with $\hat{s} = 1$ (d-1, 2), $\hat{s} = 0.5$ (e-1, 2), $\hat{s} = -1$ (e-1, 2). The other parameters used here are $L = 2$, $M = 10$, $q = 2$, $\theta_k = 0$, $\alpha = 0$, $\eta_i = 3$, $\epsilon_n = 0.3$, and $k_\theta \rho_{T_i} = 0.65$.
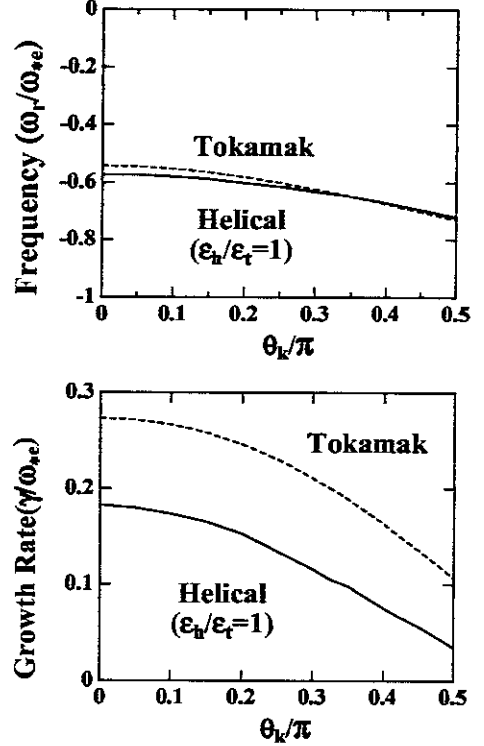
Fig. 7. Normalized real frequency ω_r/ω_{*e} (top) and growth rate γ/ω_{*e} (bottom) as a function of θ_k for $L = 2$, $M = 10$, $q = 2$, $\hat{s} = -1$, $\epsilon_h/\epsilon_t = 1$, $\alpha = 0$, $\eta_i = 3$, $\epsilon_n = 0.3$, and $k_\theta \rho_{T_i} = 0.65$. The negative shear tokamak case with the same parameters except for $\epsilon_h/\epsilon_t = 0$ is plotted by the dotted line.

3.6 Dependence on the poloidal wavenumber

Figure 10 shows the normalized real frequency $\omega_r k_\theta \rho_{T_i}/\omega_{*e}$ and the normalized growth rate $\gamma k_\theta \rho_{T_i}/\omega_{*e}$ of the helical ITG mode as a function of the normalized poloidal wavenumber $k_\theta \rho_{T_i}$. Here, we employ $\omega_{*e}(k_\theta \rho_{T_i})^{-1}$ as the normalization unit for the frequency in order to remove the wavenumber dependence from the unit. For the LHD case mentioned earlier, we obtain $\omega_{*e}(k_\theta \rho_{T_i})^{-1} = 2.77 \times 10^5 sec^{-1}$. The parameters used here are the same as the standard ones (see the first paragraph of this section) except for $k_\theta \rho_{T_i}$. With increasing $k_\theta \rho_{T_i}$, the real frequency keeps its negative sign (the ion diamagnetic rotation) and its absolute value increases monotonically. We find the lower and upper boundaries in the poloidal wavenumber region for unstable modes ($\gamma > 0$). The maximum of the growth rate is given around $k_\theta \rho_{T_i} \simeq 0.65$, and this is why this poloidal wavenumber is taken as the standard one for the calculations in the previous subsections. The stable modes, which exist in the low and high poloidal wavenumber regions, are considered to play the role of the energy sink, which is necessary for the nonlinear saturation of the ITG modes.

3.7 Temperature gradient effects

Figure 11 shows the normalized real frequency ω_r/ω_{*e} and growth rate γ/ω_{*e} as a function of η_i. The parameters used here are the same as the standard ones (see the first paragraph of this section) except for η_i. As η_i increases, both the growth rate and the absolute value of the real frequency increase monotonically. Since our numerical code can calculate both positive and negative growth rates by proper analytic continuation of the dispersion relation, we can clearly identify the critical η_i value η_{ic} for which the growth rate vanishes.

3.8 Density gradient effects

Let us recall that the parameter $\epsilon_n = L_n/R = -n_0/(R\ dn_0/dr)$ is inversely proportional to the density gradient. Thus, we investigate the density gradient dependence of the ITG mode properties by varying ϵ_n. Hollow density profiles are often observed in helical systems. Then, there exists a core plasma region, in which $dn/dr > 0$ and accordingly $\epsilon_n < 0$. Here, both cases with positive and negative ϵ_n are considered. Since the density gradient also appears in the
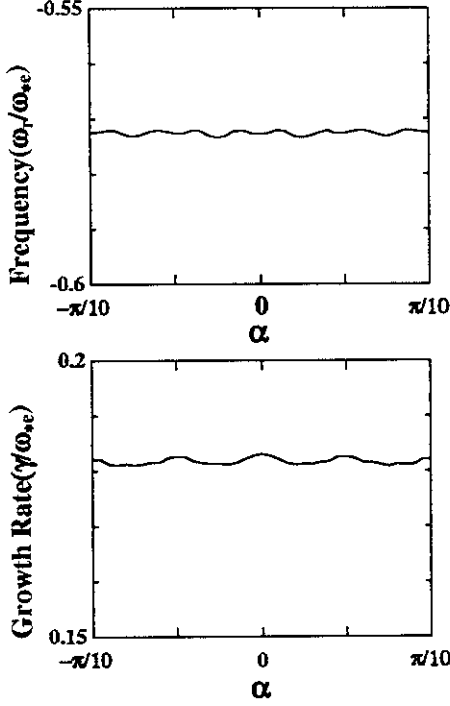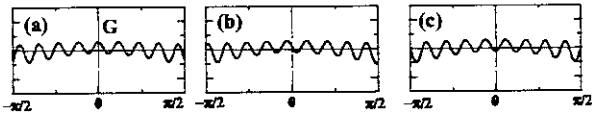
Fig. 8. Normalized real frequency ω_r/ω_{*e} (top) and growth rate γ/ω_{*e} (bottom) as a function of the field line label α for $L = 2$, $M = 10$, $q = 2$, $\hat{s} = -1$, $\epsilon_h/\epsilon_t = 1$, $\theta_k = 0$, $\eta_i = 3$, $\epsilon_n = 0.3$, and $k_\theta \rho_{Ti} = 0.65$. The negative shear tokamak case with the same parameters except for $\epsilon_h/\epsilon_t = 0$ is plotted by the dotted line.

Fig. 10. Normalized real frequency $k_\theta \rho_{Ti} \omega_r/\omega_{*e}$ (top) and growth rate $k_\theta \rho_{Ti} \gamma/\omega_{*e}$ (bottom) as a function of the normalized poloidal wavenumber $k_\theta \rho_{Ti}$ for $L = 2$, $M = 10$, $q = 2$, $\hat{s} = -1$, $\epsilon_h/\epsilon_t = 1$, $\theta_k = 0$, $\alpha = 0$, $\eta_i = 2,3,4$, and $\epsilon_n = 0.3$.

Fig. 9. Curvature factor $G(\theta)$ for $\alpha = 0$ (a), $\alpha = \pi/20$ (b), and $\alpha = \pi/10$ (c). For these values of α, the phases of $G(\theta = 0)$ are different although the connection lengths between adjacent good and bad curvature regions are almost the same. The other parameters used here are $L = 2$, $M = 10$, $\epsilon_h/\epsilon_t = 1$, $q = 2$, $\hat{s} = -1$, $\theta_k = 0$, $\alpha = 0$, $\eta_i = 3$, $\epsilon_n = 0.3$, and $k_\theta \rho_{Ti} = 0.65$.

definition of $\eta_i = L_n/L_{Ti}$, we impose the constraint $\eta_i/\epsilon_n = R/L_{Ti} = 10$ to fix the temperature gradient. This constraint $\eta_i/\epsilon_n = R/L_{Ti} = 10$ is chosen since it is given for the case of the standard parameters. The parameters used here are the same as the standard ones (see the first paragraph of this section) except for ϵ_n and η_i. The density gradient effects are shown in Fig. 12, where the normalized real frequency $\omega_r/(\omega_{*e}\epsilon_n)$ and the normalized growth rate $\gamma/(\omega_{*e}\epsilon_n)$ are shown as a function of ϵ_n. Here, we employ the new normalization unit $\omega_{*e}\epsilon_n$ in order to remove the density gradient dependence from the unit. We should note that the ϵ_n variation from $\epsilon_n = +0$ (-0) to $\epsilon_n = +\infty$ ($-\infty$) corresponds to the density gradient variation from $dn_0/dr = -\infty$ ($+\infty$) to $dn_0/dr = -0$ ($+0$). We find from Fig. 12 that the growth rate has a peak at the negative density gradient with $\epsilon_n = 0.23$ for the helical case ($\epsilon_n = 0.27$ for the tokamak case). For more flattened negative density gradient $\epsilon_n > 0.23$, the growth rate becomes smaller. Furthermore, increasing the density gradient from $dn_0/dr = +0$ to $+\infty$, the growth rate continues to decrease. Similar ϵ_n-dependence of the real frequency is found although it has no peak in the region $\epsilon_n > 0$. The hollow density profile is considered to be more stable against the ITG mode than the normal profile with the same temperature
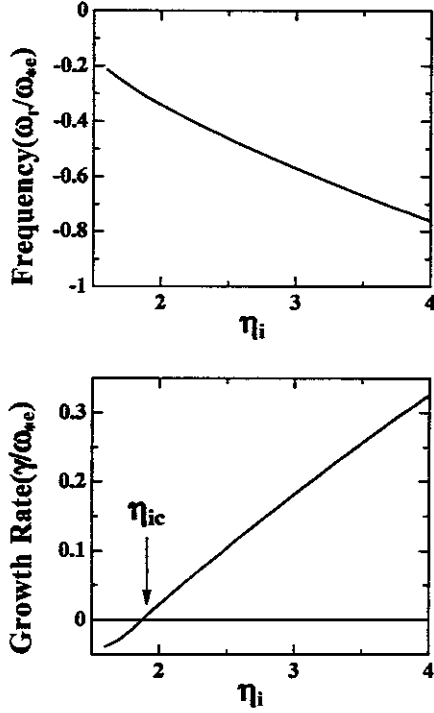
Fig. 11. Normalized real frequency ω_r/ω_{*e} (top) and growth rate γ/ω_{*e} (bottom) as a function of η_i for $L = 2$, $M = 10$, $q = 2$, $\hat{s} = -1$, $\epsilon_h/\epsilon_t = 1$, $\theta_k = 0$, $\alpha = 0$, $\epsilon_n = 0.3$, and $k_\theta \rho_{Ti} = 0.65$.
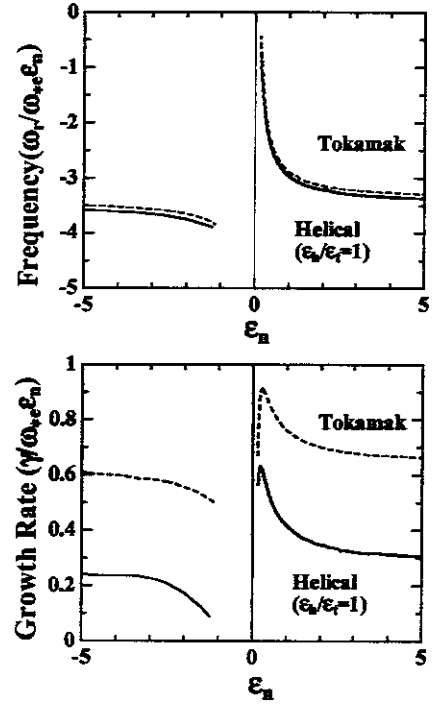
Fig. 12. Normalized real frequency $\omega_r/(\omega_{*e}\epsilon_n)$ (top) and growth rate $\gamma/(\omega_{*e}\epsilon_n)$ (bottom) as a function of ϵ_n under the constraint $\eta_i/\epsilon_n = -[T_i^{-1}dT_i/dr]R = 10$ for $L = 2$, $M = 10$, $q = 2$, $\hat{s} = -1$, $\epsilon_h/\epsilon_t = 1$, $\theta_k = 0$, $\alpha = 0$, and $k_\theta \rho_{Ti} = 0.65$. The negative shear tokamak case with the same parameters except for $\epsilon_h/\epsilon_t = 0$ is plotted by the dotted line. Here, the ϵ_n variation from $\epsilon_n = +0$ (−0) to $\epsilon_n = +\infty$ (−∞) corresponds to the density gradient variation from $dn_0/dr = -\infty$ (+∞) to $dn_0/dr = -0$ (+0).

gradient. Using the dimensional parameters at the magnetic surface $r/a = 0.6$ of the typical NBI-heated plasma in LHD with the flat density profile ($\epsilon_n = L_n/R \to \infty$), the real frequency and growth rate of the ITG mode are evaluated from Fig. 12 ($\omega_{*e}\epsilon_n = 0.54 \times 10^5 sec^{-1}$) as $\omega_r = -1.9 \times 10^5 sec^{-1}$ and $\gamma = 1.6 \times 10^4 sec^{-1}$, respectively.

§4. Conclusions

In this work, we have investigated the linear ITG modes in helical systems. Using the ion gyrokinetic equation, the adiabatic electron assumption, and the quasineutrality condition, the ITG mode dispersion relation is derived as an integral equation, where effects of toroidal and helical magnetic ripples are taken into account through the ion ∇B-curvature drift frequency. By numerically solving the integral equation with the proper analytic continuation performed, the real frequency, growth rate, and eigenfunction are obtained for both stable and unstable cases. The numerical results have shown dependences of these linear ITG mode properties on various parameters including the helical ripple intensity, safety factor, magnetic shear, ballooning angle, poloidal wavenumber, temperature and density gra-

dients. Typical parameter values used here are given by considering the LHD experiment. Also, the characteristics of the ITG mode in the helical system are compared with those for the tokamak case with the same parameters except for no helical ripples.

Due to the helical ripples, the connection lengths between adjacent good and bad curvature regions are reduced, and the good curvature regions also appear even in the outside of the torus. Then, the ITG modes for the case of finite helical ripples are more stable than for the corresponding tokamak case. The eigenfunctions for the helical case spread in the whole torus outside region like those for the tokamak case, although the former are rippled by the helical magnetic structure. For both tokamak and helical cases, the negative magnetic shear reduces the bad curvature region and accordingly the growth rate.

The field line label effects are not so obvious as the stabilizing effects of varying the ballooning angle parameter. Stronger dependence on the field line label may happen if we consider other effects such as the Shafranov shift

which are not included in our magnetic field model here In order to treat this problem more accurately, more detailed magnetic field model should be used. Also, effects of nonadiabatic electrons, trapped ions, collisions, impurities, and sheared radial electric fields, which are not treated in this work, remain as future problems. However, we believe that the results obtained here give the basics of further studies on microinstabilities in helical systems.

Acknowledgements

1) W. Horton: Rev. Mod. Phys. **71** (1999) 735.
2) W. Horton, M. Wakatani, and A. J. Wooton: in *Ion Temperature Gradient Driven Turbulent Transport*, (American Institute of Physics, New York, 1994).
3) A. Iiyoshi, *et al.*: Nucl. Fusion **39** (1999).
4) N. Ohyabu, *et al.*: to be published in Journal of Plasma and Fusion Research [in Japanese].
5) L. I Rudakov and R. Z. Sagdeev: Sov. Phys.-Dokl. **6** (1961) 415.
6) J. Y. Kim and W. Horton: Phys. Fluids B **3** (1991) 1167.
7) N. Nishimura, *et al.*: Fusion Technol. **17** (1990) 86.
8) P. H. Rutherford and E. A. Frieman: Phys. Fluids **11** (1968) 569.
9) J. B. Taylor and R. J. Hastie: Plasma Phys. **10** (1968) 479 .
10) J. L. V. Lewandowski: Plasma Phys. Control. Fusion **40** (1998) 283.
11) G. Rewoldt, L.-P. Ku, W. M. Tang, and W. A. Cooper: Phys. Plasmas **6** (1999) 4705.
12) J. Q. Dong, W. Horton, and J. Y. Kim: Phys. Fluids B **4** (1992) 1867.
13) F. Romanelli, Phys. Fluids B **1** (1989) 1018.
14) R. D. Hazeltine and J. D. Meiss: *Plasma Confinement* (Addison-Wesley, Redwood City, California, 1992), p. 298.
15) R. L. Dewar and A. H. Glasser: Phys. Fluids **26** (1983) 3038.
16) J. Y. Kim, Y. Kishimoto, W. Horton, and T. Tajima, Phys. Plasmas **1** (1994) 927.
17) T. Kuroda, H. Sugama, R. Kanno, M. Okamoto, and W. Horton, J. Phys. Soc. Jpn. **67** (1998) 3787.
18) H. Sugama: Phys. Plasmas **6** (1999) 3527.
19) M. Fujiwara, *et al.*: Nucl. Fusion **39** (1999) 1659.
20) J. Y. Kim and M. Wakatani: Phys. Plasmas **2** (1995) 1012.
21) J. Q. Dong, Y. Z. Zhang, S. M. Mahajan, and P N. Guzdar: Phys. Plasmas **3** (1996) 3065.
22) W. A. Cooper: Plasma Phys. Controlled Fusion **30** (1988) 1805.
23) J. B. Taylor and H. R. Wilson: Plasma Phys. Control. Fusion **38** (1996) 1999.
24) H. Sugama and W. Horton: in *Two-dimensional Turbulence in Plasmas and Fluids*, edited by R. L. Dewar and R. W. Griffiths (American Institute of Physics, New York, 1997), p. 275.
25) G. Rewoldt, L. L. Lao, and W. M. Tang: Phys. Plasmas **4** (1997) 3293

Recent Issues of NIFS Series

5D Simulation Study of Suprathermal Electron Transport in Non-Axisymmetric Plasmas;Oct. 1998
(IAEA-CN-69/THP1/01)

NIFS-577   S. Fujiwara and T. Sato,
            Molecular Dynamics Simulation of Structure Formation of Short Chain Molecules; Nov. 1998

NIFS-578   T. Yamagishi,
            Eigenfunctions for Vlasov Equation in Multi-species Plasmas Nov. 1998

NIFS-579   M. Tanaka, A. Yu Grosberg and T. Tanaka,
            Molecular Dynamics of Strongly-Coupled Multichain Coulomb Polymers in Pure and Salt Aqueous Solutions; Nov. 1998

NIFS-580   J. Chen, N. Nakajima and M. Okamoto,
            Global Mode Analysis of Ideal MHD Modes in a Heliotron/Torsatron System: I. Mercier-unstable Equilibria; Dec. 1998

NIFS-581   M. Tanaka, A. Yu Grosberg and T. Tanaka,
            Comparison of Multichain Coulomb Polymers in Isolated and Periodic Systems: Molecular Dynamics Study; Jan. 1999

NIFS-582   V.S. Chan and S. Murakami,
            Self-Consistent Electric Field Effect on Electron Transport of ECH Plasmas; Feb. 1999

NIFS-583   M. Yokoyama, N. Nakajima, M. Okamoto, Y. Nakamura and M. Wakatani,
            Roles of Bumpy Field on Collisionless Particle Confinement in Helical-Axis Heliotrons, Feb. 1999

NIFS-584   T.-H. Watanabe, T. Hayashi, T. Sato, M. Yamada and H. Ji,
            Modeling of Magnetic Island Formation in Magnetic Reconnection Experiment; Feb. 1999

NIFS-585   R. Kumazawa, T. Mutoh, T. Seki, F. Shinpo, G. Nomura, T. Ido, T. Watari, Jean-Marie Noterdaeme and Yangping Zhao,
            Liquid Stub Tuner for Ion Cyclotron Heating; Mar. 1999

NIFS-586   A. Sagara, M. Iima, S. Inagaki, N. Inoue, H. Suzuki, K. Tsuzuki, S. Masuzaki, J. Miyazawa, S. Morita, Y. Nakamura, N. Noda, B. Peterson, S. Sakakibara, T. Shimozuma, H. Yamada, K. Akaishi, H. Chikaraishi, H. Funaba, O. Kaneko, K. Kawahata, A. Komori, N. Ohyabu, O. Motojima, LHD Exp. Group 1, LHD Exp. Group 2,
            Wall Conditioning at the Starting Phase of LHD; Mar. 1999

NIFS-587   T. Nakamura and T. Yabe,
            Cubic Interpolated Propagation Scheme for Solving the Hyper-Dimensional Vlasov-Poisson Equation in Phase Space; Mar. 1999

NIFS-588   W.X. Wnag, N. Nakajima, S. Murakami and M. Okamoto,
            An Accurate δf Method for Neoclassical Transport Calculation ; Mar. 1999

NIFS-589   K. Kishida, K. Araki, S. Kishiba and K. Suzuki,
            Local or Nonlocal? Orthonormal Divergence-free Wavelet Analysis of Nonlinear Interactions in Turbulence; Mar. 1999

NIFS-590   K. Araki, K. Suzuki, K. Kishida and S. Kishiba,
            Multiresolution Approximation of the Vector Fields on T^3; Mar. 1999

NIFS-591   K. Yamazaki, H. Yamada, K.Y.Watanabe, K. Nishimura, S. Yamaguchi, H. Nakanishi, A. Komori, H. Suzuki, T. Mito, H. Chikaraishi, K.Murai, O. Motojima and the LHD Group,
            Overview of the Large Helical Device (LHD) Control System and Its First Operation; Apr. 1999

NIFS-592   T. Takahashi and Y. Nakao,
            Thermonuclear Reactivity of D-T Fusion Plasma with Spin-Polarized Fuel; Apr. 1999

NIFS-593   H. Sugama,
            Damping of Toroidal Ion Temperature Gradient Modes; Apr. 1999

NIFS-594   Xiaodong Li,
            Analysis of Crowbar Action of High Voltage DC Power Supply in the LHD ICRF System; Apr. 1999

NIFS-595   K. Nishimura, R. Horiuchi and T. Sato,

Drift-kink Instability Induced by Beam Ions in Field-reversed Configurations, Apr 1999

NIFS-596   Y. Suzuki, T-H Watanabe, T. Sato and T. Hayashi,

Three-dimensional Simulation Study of Compact Toroid Plasmoid Injection into Magnetized Plasmas;
Apr 1999

NIFS-597   H. Sanuki, K. Itoh, M. Yokoyama, A. Fujisawa, K. Ida, S. Toda, S-I. Itoh, M. Yagi and A. Fukuyama,
Possibility of Internal Transport Barrier Formation and Electric Field Bifurcation in LHD Plasma,
May 1999

NIFS-598   S. Nakazawa, N. Nakajima, M. Okamoto and N. Ohyabu,
One Dimensional Simulation on Stability of Detached Plasma in a Tokamak Divertor, June 1999

NIFS-599   S. Murakami, N. Nakajima, M. Okamoto and J. Nhrenberg,
Effect of Energetic Ion Loss on ICRF Heating Efficiency and Energy Confinement Time in Heliotrons,
June 1999

NIFS-600   R. Honuchi and T. Sato,
*Three-Dimensional Particle Simulation of Plasma Instabilities and Collisionless Reconnection in a
Current Sheet,*, June 1999

NIFS-601   W. Wang, M. Okamoto, N. Nakajima and S. Murakami,
Collisional Transport in a Plasma with Steep Gradients; June 1999

NIFS-602   T. Mutoh, R. Kumazawa, T. Saki, K. Saito, F. Simpo, G. Nomura, T. Watari, X. Jikang, G. Cattanei, H. Okada, K. Ohkubo, M. Sato,
S. Kubo, T. Shimozuma, H. Idei, Y. Yoshimura, O. Kaneko, Y. Takeiri, M. Osakabe, Y. Oka, K. Tsumori, A. Komori, H. Yamada, K.
Watanabe, S. Sakakibara, M. Shoji, R. Sakamoto, S. Inagaki, J. Miyazawa, S. Morita, K. Tanaka, B.J. Peterson, S. Murakami, T.
Minami, S. Ohdachi, S. Kado, K. Narihara, H. Sasao, H. Suzuki, K. Kawahata, N. Ohyabu, Y. Nakamura, H. Funaba, S. Masuzaki,
S. Muto, K. Sato, T. Morisaki, S. Sudo, Y. Nagayama, T. Watanabe, M. Sasao, K. Ida, N. Noda, K. Yamazaki, K. Akaishi, A.
Sagara, K. Nishimura, T. Ozaki, K. Toi, O. Motojima, M. Fujiwara, A. liyoshi and LHD Exp Group 1 and 2,
First ICRF Heating Experiment in the Large Helical Device ; July 1999

NIFS-603   P.C. de Vries, Y. Nagayama, K. Kawahata, S. Inagaki, H. Sasao and K. Nagasaki,
Polarization of Electron Cyclotron Emission Spectra in LHD; July 1999

NIFS-604   W. Wang, N. Nakajima, M. Okamoto and S. Murakami,
δf Simulation of Ion Neoclassical Transport; July 1999

NIFS-605   T. Hayashi, N. Mizuguchi, T. Sato and the Complexity Simulation Group,
Numerical Simulation of Internal Reconnection Event in Spherical Tokamak; July 1999

NIFS-606   M. Okamoto, N. Nakajima and W. Wang,
On the Two Weighting Scheme for δf Collisional Transport Simulation; Aug. 1999

NIFS-607   O. Motojima, A.A. Shishkin, S. Inagaki, K.Y. Watanabe,
Possible Control Scenario of Radial Electric Field by Loss-Cone-Particle Injection into Helical Device; Aug.
1999

NIFS-608   R. Tanaka, T. Nakamura and T. Yabe,
Constructing Exactly Conservative Scheme in Non-conservative Form ; Aug. 1999

NIFS-609   H. Sugama,
Gyrokinetic Field Theory, Aug. 1999

NIFS-610   M. Takechi, G. Matsunaga, S. Takagi, K.Ohkuni, K. Toi, M. Osakabe, M. Isobe, S. Okamura, K. Matsuoka, A. Fujisawa, H. Iguchi,
S. Lee, T. Minami, K. Tanaka, Y. Yoshimura and CHS Group,
*Core Localized Toroidal Alfven Eigenmodes Destabilized By Energetic Ions in the CHS
Heliotron/Torsatron*; Sep. 1999

NIFS-611   K. Ichiguchi,
MHD Equilibrium and Stability in Heliotron Plasmas, Sep. 1999

NIFS-612   Y. Sato, M. Yokoyama, M. Wakatani and V. D. Pusovitov,
Complete Suppression of Pfirsch-Schluter Current in a Toroidal l=3 Stellarator; Oct. 1999

NIFS-613   S. Wang, H. Sanuki and H. Sugama,

Reduced Drift Kinetic Equation for Neoclassical Transport of Helical Plasmas in Ultra-low Collisionality Regime;Oct. 1999

NIFS-614   J. Miyazawa, H. Yamada, K. Yasui, S. Kato, N., Fukumoto, M. Nagata and T. Uyama,
Design of Spheromak Injector Using Conical Accelerator for Large Helical Device,Nov. 1999

NIFS-615   M. Uchida, A. Fukuyama, K. Itoh, S.-I. Itoh and M. Yagi,
Analysis of Current Diffusive Ballooning Mode in Tokamaks, Dec. 1999

NIFS-616   M. Tanaka, A.Yu Grosberg and T. Tanaka,
Condensation and Swelling Behavior of Randomly Charged Multichain Polymers by Molecular Dynamics Simulations; Dec. 1999

NIFS-617   S. Goto and S. Kida,
Sparseness of Nonlinear Coupling; Dec 1999

NIFS-618   M.M. Skoric, T. Sato, A. Maluckov and M.S. Jovanovic,
Complexity in Laser Plasma Instabilities Dec. 1999

NIFS-619   T.-H. Watanabe, H. Sugama and T. Sato,
Non-dissipative Kinetic Simulation and Analytical Solution of Three-mode Equations of Ion Temperature Gradient Instability; Dec. 1999

NIFS-620   Y. Oka, Y. Takeiri, Yu.I Belchenko, M. Hamabe, O. Kaneko, K. Tsumori, M. Osakabe, E. Asano, T. Kawamoto, R. Akiyama,
Optimization of Cs Deposition in the 1/3 Scale Hydrogen Negative Ion Source for LHD-NBI System ;Dec. 1999

NIFS-621   Yu.I. Belchenko, Y. Oka, O. Kaneko, Y. Takeiri, A. Krivenko, M. Osakabe, K. Tsumori, E. Asano, T. Kawamoto, R. Akiyama,
Recovery of Cesium in the Hydrogen Negative Ion Sources;Dec. 1999

NIFS-622   Y. Oka, O. Kaneko, K. Tsumori, Y. Takeiri, M. Osakabe, T. Kawamoto, E. Asano, and R. Akiyama,
H- Ion Source Using a Localized Virtual Magnetic Filter in the Plasma Electrode: Type I LV Magnetic Filter: Dec. 1999

NIFS-623   M. Tanaka, S Kida, S. Yanase and G. Kawahara,
Zero-absolute-vorticity State in a Rotating Turbulent Shear Flow;Jan 2000

NIFS-624   F. Leuterer, S. Kubo,
Electron Cyclotron Current Drive at $\omega \approx \omega_c$ with X-mode Launched from the Low Field Side; Feb 2000

NIFS-625   K. Nishimura,
Wakefield of a Charged Particulate Influenced by Emission Process of Secondary Electrons; Mar. 2000

NIFS-626   K. Itoh, M. Yagi, S.-I Itoh, A. Fukuyama,
On Turbulent Transport in Burning Plasmas;Mar 2000

NIFS-627   K. Itoh, S.-I. Itoh, L. Giannone,
Modelling of Density Limit Phenomena in Toroidal Helical Plasmas, Mar. 2000

NIFS-628   K. Akaishi, M. Nakasuga and Y. Funato,
True and Measured Outgassing Rates of a Vacuum Chamber with a Reversibly Absorbed Phase,Mar. 2000

NIFS-629   T. Yamagishi,
Effect of Weak Dissipation on a Drift Orbit Mapping, Mar. 2000

NIFS-630   S. Toda, S.-I, Itoh, M. Yagi, A. Fukuyama and K. Itoh,
Spatial Structure of Compound Dither in L/H Transition;Mar. 2000

NIFS-631   N. Ishihara and S. Kida,
Axial and Equatorial Magnetic Dipoles Generated in a Rotating Spherical Shell; Mar. 2000

NIFS-632   T. Kuroda, H. Sugama, R. Kanno and M. Okamoto,
Ion Temperature Gradient Modes in Toroidal Helical Systems; Apr. 2000